Materials International
Open-Access Journal (ISSN: 2668-5728)

*Article*
**Volume 7, Issue 3, 2025, 27**
https://doi.org/10.33263/Materials73.027

# Formation of Chromium-Silicon Carbide Microparticles for Trapping NO, CO, $NO_2$, $CO_2$: A Step Forward to Green Chemistry through Designing of Gas Adsorption

**Fatemeh Mollaamin** [1,*]

[1] Department of Biomedical Engineering, Faculty of Engineering and Architecture, Kastamonu University, Kastamonu, Turkey
* Correspondence: fmollaamin@kastamonu.edu.tr;

**Received: 28.12.2024; Accepted: 30.07.2025; Published: 10.09.2025**

**Abstract:** Silicon Carbide (SiC) monolayer, as a new graphene-like semiconductor, is a direct band gap material. Thermochemical, electric, and magnetic properties of chromium (Cr) metal-doped graphene-like SiC monolayer sheet are studied by the first-principles methods based on the density functional theory (DFT) for scavenging of CO, $CO_2$, NO, and $NO_2$ gas molecules. The results recommend that the adsorption of these gas molecules on the Cr-embedded SiC sheet monolayer is more energetically desired than that on the pristine ones. Gas molecules of CO, $CO_2$, NO, and $NO_2$ have been adsorbed on the Cr site of the doped SiC monolayer through the formation of covalent bonds. The assumption of chemical adsorptions has been approved by the projected density of states (PDOS) and charge density difference plots. Charge density difference calculations also indicate that the electronic densities were mainly accumulated on the adsorbate of CO, $CO_2$, NO, and $NO_2$ gas molecules. The results of this investigation indicate the competence of transition-metal-doped silicon carbide nanosheets in gas adsorption systems.

**Keywords:** gas adsorption; CO, $CO_2$, NO, $NO_2$; silicon carbide; simulation method.



## 1. Introduction

Graphene, with its two-dimensional (2D) layered physical structure and unique electronic properties, has sparked broad research interest in 2D materials, which can be applied to electronic, optoelectronic, and spintronic devices [1–5].

But the practical application of 2D materials like graphene might be confined to a small band gap. Thus, new 2D materials with perfect mechanical, thermoelectric, optical, and electronic properties are the clue to the recent scientific investigations [6–14].

The Silicon Carbide (SiC) monolayer, as a new graphene-like semiconductor, is a direct-band-gap material, while silicon, in the same group as carbon, shares attributes entirely analogous to those of carbon and enables powerful applications in optoelectronic and electronic instruments [15–20].

In addition, transition metal (TM) atoms are considered the source of magnetism; in TM-doped SiC monolayers, the system can be a magnetic semiconductor upon Co, Cu, Fe, Mn, and Ni doping [21]. The TM dopants can cause a total Hamiltonian perturbation, eventually

leading to changes in electronic structures, which makes it a substantial application in magnetic electronic devices [22–28].

In this work, we shall present theoretical estimates of charge transfer and binding energy to the SiC surface for molecular adsorption. Let us note that there are also model approaches to the problem of adsorption, in addition to the popular and currently widely used first-principles calculations. Then, the magnetic and electronic structures of Cr–doped graphene-like SiC sheet through adsorption of CO, $CO_2$, NO, $NO_2$ gas molecules (GM→CrSiC) by using first-principle calculations based on the density functional theory (DFT) [29]. The calculation is performed using the generalized gradient approximation (GGA) potential and the Perdew-Burke-Ernzerhof (PBE) functional [30, 31].

## 2. Materials and Methods

The adsorption of CO, $CO_2$, NO, and $NO_2$ gas molecules on the surface of CrSiC was defined by the theory of the "Langmuir" isotherm, which indicates the chemisorption between gas molecules and CrSiC. The adsorbates of CO, $CO_2$, NO, and $NO_2$ gas molecules are maintained on the surface of CrSiC with "Langmuir" chemisorption [32–38] (Figure 1).

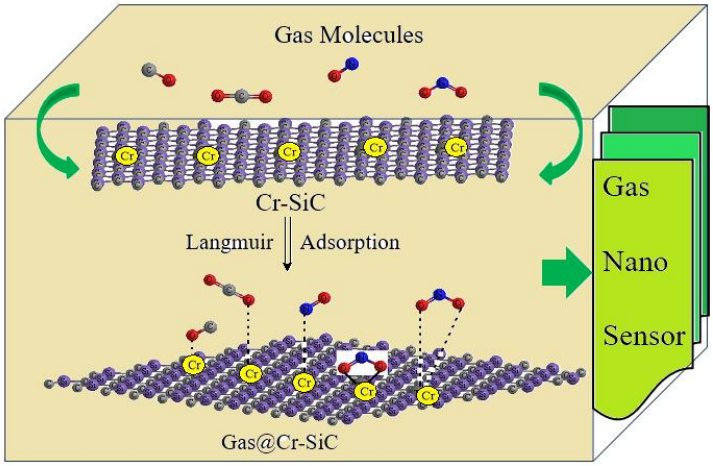


**Figure 1.** A simulated box of Langmuir adsorption of CO, $CO_2$, NO, and $NO_2$ onto Cr–doped SiC nanosheet towards the formation of gas adsorption.

In this research, the simulated calculations have been performed in GaussView 6.06.16 [39] and calculated by Gaussian 16, Revision C.01 [40] using the DFT method. The [Perdew–Burke–Ernzerhof] "PBE" functional with high-precision generalized gradient approximation "GGA" has been employed to achieve more authentic results [30].

After organizing the structure and energetics of the SiC sheet, we have tried to decorate the sheet with chromium atoms. A full geometry optimization has been performed, and the data show that the most stable location of chromium is on the top of the Si atom, with it pushed down into the surface.

After doping chromium on the silicon atom, the planarity of the system is perturbed because the silicon atom goes toward the $sp^3$ hybridization. Although silicon and carbon atoms are iso-valent, the most stable state of carbon is $sp^2$, and silicon is $sp^3$ [41,42].

The interaction of CO, $CO_2$, NO, and $NO_2$ gas molecules with the Cr-decorated SiC sheet. The optimized geometries of the GM→Cr– decorated SiC sheet are shown in Figure 1.

The changes of charge density analysis in the adsorption process have illustrated that CrSiC shows the Bader charge of –1.308e before adsorption of CO, $CO_2$, NO, $NO_2$, and –

1.314e, –1.304e, –1.319e, –1.322e after adsorption of CO, $CO_2$, NO, $NO_2$, respectively. Therefore, the changes of charge density for "Langmuir" adsorption of CO, $CO_2$, NO, $NO_2$ on CrSiC surface alternatively are $\Delta Q_{CO2 \rightarrow CrSiC}$ = +0.004e >$\Delta Q_{CO \rightarrow CrSiC}$ = –0.006e > $\Delta Q_{NO \rightarrow CrSiC}$ = –0.011e > $\Delta Q_{NO2 \rightarrow CrSiC}$ = –0.014e. The values of changes of charge density have shown a more important charge transfer for CrSiC, which acts as the electron acceptor, while gas molecules act as the stronger electron donors through adsorption on the CrSiC surface [43–46].

The simulated distribution functions of NO → CrSiC, $NO_2$ → CrSiC, CO → CrSiC, and $CO_2$ → CrSiC have illustrated that the created clusters lead to the bond lengths of N → Cr in NO → CrSiC (2.07 Å), O → Cr in $NO_2$ → CrSiC ( 2.06 Å), O → Cr in CO → CrSiC ( 2.05 Å), and O → Cr in $CO_2$ → CrSiC ( 2.05 Å) (Figure 1).

## 3. Results and Discussion

In this verdict, chromium (Cr) metal-doped graphene-like silicon carbide (SiC) monolayer sheet has been investigated as an efficient surface because of its structural selectivity for the adsorption of carbon monoxide (CO), carbon dioxide ($CO_2$), nitric oxide (NO), and nitrogen dioxide ($NO_2$). These experiments have been conducted using spectroscopic analysis of physical and chemical properties.

### *3.1. Electronic properties.*

The electronic structures of CO, $CO_2$, NO, and $NO_2$ adsorbed on the Cr–doped SiC nanosheet (GM→ CrSiC) have been analyzed to simplify subsequent discussion for interfacial electronic properties using CAM-B3LYP/ LANL2DZ, 6-311+G (d,p) basis sets.

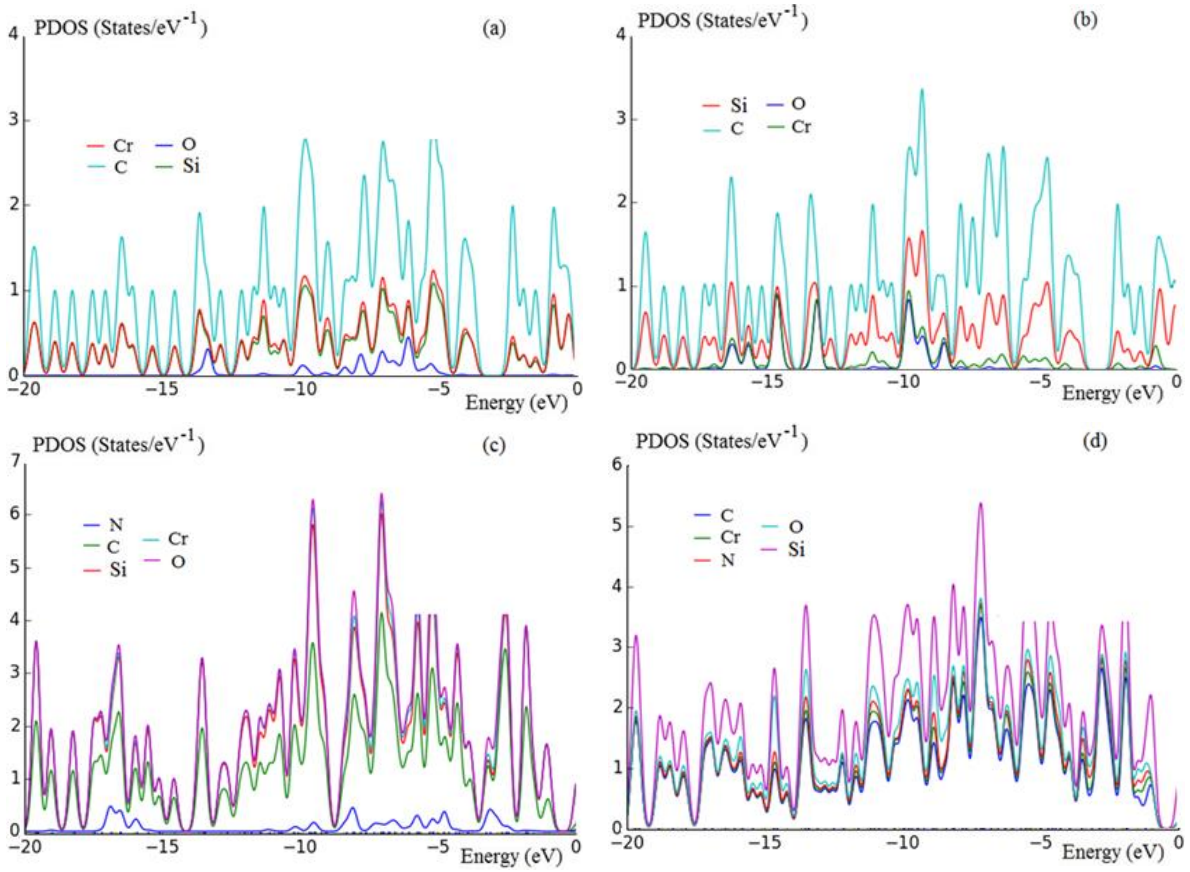


**Figure 2.** PDOS adsorption of **(a)** CO→CrSiC; **(b)** $CO_2$→ Cr–SiC; **(c)** NO→ CrSiC; **(d)** $NO_2$→ CrSiC.

Therefore, the graph of partial DOS (PDOS) has illustrated that the *p* states of the adsorption of N- and O- on the CrSiC are dominant through the conduction band (Figure 2).

A distinct metallic feature can be observed in SiC because of the strong interaction between the *p* states of C, N, O, Si, and the *d* state of Cr near the Fermi energy. Moreover, the existence of covalent features for these complexes has exhibited the same energy amount and figure of the PDOS for the *p* orbitals of C, N, O, Si, and *d* orbitals of Cr (Figure 2a-d).

Figure 2a,b shows that the CO and $CO_2$ states, respectively, onto CrSiC have more contribution at the middle of the conduction band between -5eV to -10eV, while contributions of carbon and silicon states are expanded and close together, but chromium states have minor contributions.

Figure 2c,d shows that the NO and $NO_2$ states, respectively, onto CrSiC have more contribution at the middle of the conduction band between -5eV to -10eV, while contributions of carbon and silicon states are expanded and close together, but chromium states have major contributions.

The results were also approved by the partial electron density (PDOS), which has shown a certain charge association between CrSiC and gas molecules of CO, $CO_2$, NO, and $NO_2$.

Therefore, the above results show that the dominance of non-metallic and metallic features, along with a certain degree of covalent features, can account for the increase in the semiconducting direct band gap of gas molecules (CO, CO2, NO, and NO2) adsorbed on CrSiC.

*3.2. NQR "Nuclear quadrupole resonance" analysis.*

NQR procedure has been done for the complexes of gas molecules of CO, $CO_2$, NO, and $NO_2$ adsorbing on CrSiC. NQR is related to the multipole enlargement in Cartesian harmonies as follows [47,48]:

$$V(r) = V(0) + \left[\left(\frac{\partial V}{\partial x_i}\right)\Big|_0 . x_i\right] + \frac{1}{2}\left[\left(\frac{\partial^2 V}{\partial x_i x_j}\right)\Big|_0 . x_i x_j\right] \quad (1)$$

$$U = -\frac{1}{2}\int_{\mathcal{D}} d^3\, r\, \rho_r \left[\left(\frac{\partial^2 V}{\partial x_i^2}\right)\Big|_0 . x_i^2\right] = -\frac{1}{2}\int_{\mathcal{D}} d^3\, r\, \rho_r \left[\left(\frac{\partial E_i}{\partial x_i}\right)\Big|_0 . x_i^2\right] = -\frac{1}{2}\left(\frac{\partial E_i}{\partial x_i}\right)\Big|_0 . \int_{\mathcal{D}} d^3\, r\, [\rho(r) . x_i^2] \quad (2)$$

There are two factors which should be obtained from nuclear quadrupole resonance experiments: the quadrupole coupling constant, χ, and the asymmetry factor of the electric field gradient tensor, η:

$$\chi = {e^2 Q q_{zz}}/{h} \quad (3)$$

$$\eta = {q_{xx} - q_{yy}}/{q_{zz}} \quad (4)$$

While $q_{ii}$ are ingredients of the electric field gradient tensor at the quadrupole nucleus assigned in the electric field gradient principal axes system, e is the proton charge, h is Planck's constant, and Q is the nuclear quadrupole moment [49, 50]. Since the electric field gradient at the situation of CO, $CO_2$, NO, and $NO_2$ adsorbed on the CrSiC surface, as the gas detector is approved by the valence electrons distorted in the special connection with close nuclei of Cr–

doped SiC nanosheet, the nuclear quadrupole resonance at which transitions occur is special for NO→CrSiC and $NO_2$→CrSiC (Table 1).

**Table 1.** The electric potential ($E_p$) and Bader charge (Q) for elements involved in the adsorption mechanism of CO, $CO_2$, NO, and $NO_2$ adsorbed on the Cr–doped SiC nanosheet using "CAM-B3LYP/EPR-III, 6-311+G (d,p)" calculation extracted from the NQR method.

| CO→CrSiC | | | $CO_2$→CrSiC | | | NO→CrSiC | | | $NO_2$→CrSiC | | |
|---|---|---|---|---|---|---|---|---|---|---|---|
| **Atom** | **Q** | **$E_p$** | **Atom** | **Q** | **$E_p$** | **Atom** | **Q** | **$E_p$** | **Atom** | **Q** | **$E_p$** |
| C1 | –0.01 | –14.70 | C1 | 0.38 | –14.31 | O1 | –0.08 | –22.03 | N1 | –0.19 | –18.12 |
| O2 | –0.20 | –21.97 | O2 | –0.18 | –21.79 | N2 | –0.24 | –18.18 | O2 | –0.18 | –21.81 |
| C3 | –0.86 | –14.85 | C3 | –0.86 | –14.85 | C3 | –0.84 | –14.83 | O3 | –0.20 | –22.02 |
| Si4 | 0.81 | –48.63 | Si4 | 0.80 | –48.64 | Si4 | 0.81 | –48.63 | C4 | –0.83 | –14.82 |
| C5 | –0.83 | –14.83 | C5 | –0.83 | –14.84 | C5 | –0.82 | –14.82 | Si5 | 0.82 | –48.62 |
| Si6 | 1.14 | –48.57 | Si6 | 1.11 | –48.58 | Si6 | 1.14 | –48.57 | C6 | –0.83 | –14.82 |
| C7 | –0.81 | –14.87 | C7 | –0.83 | –14.89 | C7 | –0.82 | –14.87 | Si7 | 1.21 | –48.53 |
| C8 | –1.18 | –14.84 | C8 | –1.18 | –14.85 | C8 | –1.17 | –14.82 | C8 | –0.81 | –14.85 |
| Si9 | 1.16 | –48.58 | Si9 | 1.14 | –48.59 | Si9 | 1.17 | –48.57 | C9 | –1.11 | –14.80 |
| Si10 | 1.16 | –48.58 | Si10 | 1.15 | –48.59 | Si10 | 1.17 | –48.57 | Si10 | 1.15 | –48.56 |
| C11 | –0.85 | –14.84 | C11 | –0.86 | –14.85 | C11 | –0.83 | –14.82 | Si11 | 1.21 | –48.55 |
| C12 | –1.20 | –14.80 | C12 | –1.20 | –14.81 | C12 | –1.20 | –14.79 | C12 | –0.84 | –14.82 |
| Si13 | 0.84 | –48.62 | Si13 | 0.82 | –48.63 | Si13 | 0.84 | –48.62 | C13 | –1.20 | –14.79 |
| Si14 | 1.30 | –48.50 | Si14 | 1.28 | –48.51 | Si14 | 1.31 | –48.50 | Si14 | 0.85 | –48.61 |
| C15 | –1.16 | –14.82 | C15 | –1.18 | –14.82 | C15 | –1.16 | –14.81 | Si15 | 1.32 | –48.48 |
| C16 | –1.16 | –14.82 | C16 | –1.17 | –14.83 | C16 | –1.15 | –14.81 | C16 | –1.03 | –14.69 |
| Cr17 | 1.30 | –101.89 | Cr17 | 1.30 | –101.9 | Cr17 | 1.32 | –101.8 | C17 | –1.14 | –14.81 |
| Si18 | 1.14 | –48.57 | Si18 | 1.13 | –48.58 | Si18 | 1.15 | –48.57 | Cr18 | 1.28 | –101.90 |
| C19 | –0.82 | –14.88 | C19 | –0.83 | –14.89 | C19 | –0.82 | –14.87 | Si19 | 1.16 | –48.57 |
| C20 | –1.21 | –14.77 | C20 | –1.22 | –14.78 | C20 | –1.22 | –14.82 | C20 | –0.82 | –14.87 |
| Si21 | 0.76 | –48.66 | Si21 | 0.74 | –48.68 | Si21 | 0.81 | –48.64 | C21 | –1.22 | –14.80 |
| Si22 | 1.31 | –48.50 | Si22 | 1.30 | –48.51 | Si22 | 1.28 | –48.53 | Si22 | 0.74 | –48.67 |
| C23 | –1.25 | –14.82 | C23 | –1.26 | –14.82 | C23 | –1.25 | –14.82 | Si23 | 1.29 | –48.52 |
| C24 | –1.20 | –14.80 | C24 | –1.20 | –14.81 | C24 | –1.20 | –14.80 | C24 | –1.25 | –14.81 |
| Si25 | 1.30 | –48.50 | Si25 | 1.29 | –48.51 | Si25 | 1.31 | –48.50 | C25 | –1.20 | –14.79 |
| Si26 | 0.83 | –48.63 | Si26 | 0.82 | –48.63 | Si26 | 0.85 | –48.62 | Si26 | 1.28 | –48.50 |
| C27 | –0.83 | –14.84 | C27 | –0.83 | –14.84 | C27 | –0.82 | –14.82 | Si27 | 0.84 | –48.62 |
| C28 | –0.85 | –14.77 | C28 | –0.85 | –14.79 | C28 | –0.87 | –14.80 | C28 | –0.82 | –14.82 |
| Si29 | 0.92 | –48.57 | Si29 | 0.90 | –48.59 | Si29 | 0.88 | –48.59 | C29 | –0.87 | –14.80 |
| Si30 | 0.91 | –48.58 | Si30 | 0.90 | –48.59 | Si30 | 0.92 | –48.57 | Si30 | 0.92 | –48.57 |
| C31 | –1.22 | –14.77 | C31 | –1.22 | –14.78 | C31 | –1.22 | –14.80 | Si31 | 0.87 | –48.60 |
| Si32 | 0.76 | –48.67 | Si32 | 0.74 | –48.68 | Si32 | 0.77 | –48.65 | C32 | –1.22 | –14.82 |
| | | | O33 | –0.11 | –21.81 | | | | Si33 | 0.83 | –48.63 |

Furthermore, in Figure3 (a-d) it has been drawn the electric potential of nuclear quadrupole resonance method versus Bader charge for elements of carbon, nitrogen, oxygen, silicon and chromium in the adsorption process of CO, $CO_2$, NO and $NO_2$ on the Cr– doped SiC nanosheet by "CAM-B3LYP/EPR-III, 6-311+G (d,p), LANL2DZ" theoretical level. It has been noted that changes in the electric potentials of carbon, nitrogen, oxygen, silicon, and chromium occur at the active site during Langmuir adsorption.

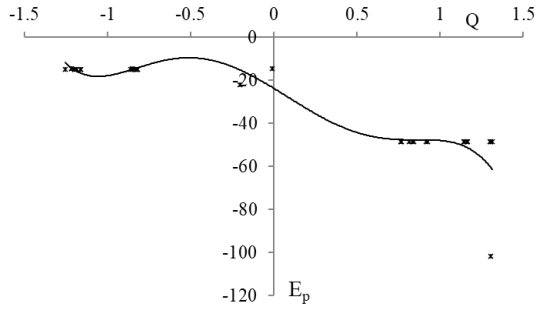


**(a)**

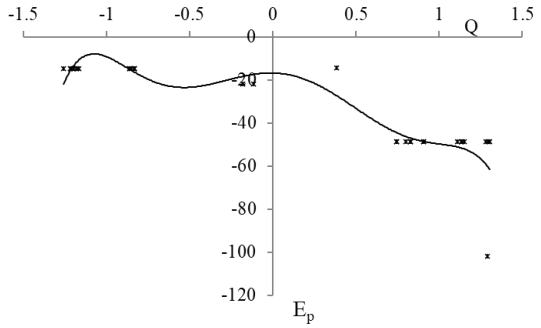


**(b)**

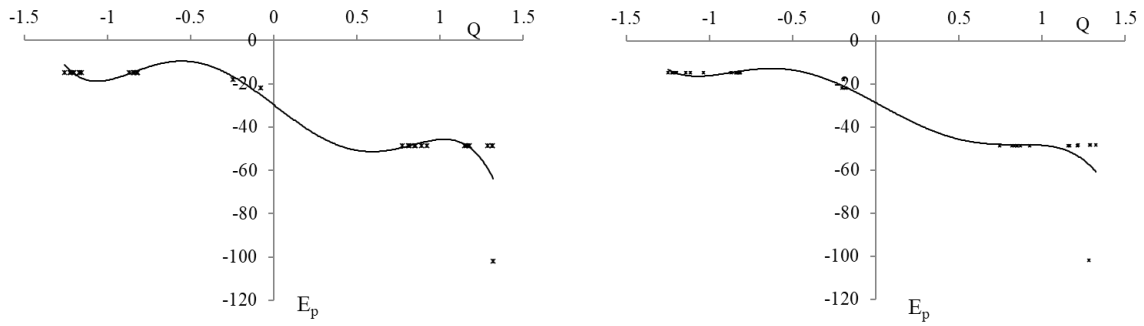


**Figure 3.** The electric potential ($E_p$) versus Bader charge (Q) for elements involved in the adsorption mechanism of CO, $CO_2$, NO, and $NO_2$ adsorbed on the Cr–doped SiC nanosheet.

In fact, it has been observed that the effect of the binding between C, N, and O atoms of gas molecules with chromium doping in the SiC nanosheet during adsorbing CO, $CO_2$, NO, and $NO_2$ results in a resulting electric potential using NQR analysis (Figure 3a-d). It's obvious that the capability of SiC nanosheet for detecting CO, $CO_2$, NO, and $NO_2$ is fluctuated by their selectivity and sensitivity, which can represent the efficiency of these surfaces as promising gas adsorption devices (Figure 3a-d).

*3.3. Magnetism of gas adsorption onto Cr-doped SiC monolayer.*

Isotropic ($\sigma_{iso}$) and anisotropy ($\sigma_{aniso}$) shielding tensors of NMR spectroscopy for certain atoms in the active site of CO, $CO_2$, NO and $NO_2$ adsorbed on the Cr –doped SiC nanosheet (GM→CrSiC) through the formation of the binding between gas molecules and solid surfaces have been calculated using Gaussian 16, Revision C.01 and reported in Tables 2 [40].

**Table 2.** Data of "GIAO/NMR" shielding tensors for selected atoms of CO, $CO_2$, NO, and $NO_2$ adsorbed on the Cr-doped SiC nanosheet (GM→CrSiC) using CAM-B3LYP/EPR-III, 6-311+G (d,p) calculation.

| **CO→CrSiC** | | | **$CO_2$→CrSiC** | | | **NO→CrSiC** | | | **$NO_2$→CrSiC** | | |
|---|---|---|---|---|---|---|---|---|---|---|---|
| **Atom** | **$\sigma_{iso}$** | **$\sigma_{aniso}$** | **Atom** | **$\sigma_{iso}$** | **$\sigma_{aniso}$** | **Atom** | **$\sigma_{iso}$** | **$\sigma_{aniso}$** | **Atom** | **$\sigma_{iso}$** | **$\sigma_{aniso}$** |
| C1 | 919.79 | 1222.39 | C1 | 104.78 | 127.69 | O1 | 2461.23 | 3517.62 | N1 | 71.59 | 420.00 |
| O2 | 156.05 | 912.93 | O2 | 320.51 | 246.55 | N2 | 623.40 | 988.10 | O2 | 285.67 | 632.05 |
| C3 | 11.73 | 506.53 | C3 | 38.53 | 441.43 | C3 | 91.71 | 263.77 | O3 | 364.23 | 675.24 |
| Si4 | 420.18 | 658.02 | Si4 | 530.63 | 420.63 | Si4 | 399.44 | 482.66 | C4 | 102.22 | 268.67 |
| C5 | 162.29 | 737.54 | C5 | 111.36 | 588.06 | C5 | 34.49 | 432.86 | Si5 | 398.08 | 465.51 |
| Si6 | 571.51 | 201.85 | Si6 | 565.47 | 145.63 | Si6 | 508.13 | 221.18 | C6 | 6.39 | 380.51 |
| C7 | 1071.14 | 1852.24 | C7 | 306.82 | 707.32 | C7 | 31.30 | 182.16 | Si7 | 538.44 | 226.51 |
| C8 | 220.83 | 683.26 | C8 | 99.24 | 246.24 | C8 | 126.21 | 189.03 | C8 | 0.53 | 209.57 |
| Si9 | 550.73 | 218.16 | Si9 | 524.97 | 226.91 | Si9 | 492.16 | 193.31 | C9 | 109.80 | 187.10 |
| Si10 | 561.66 | 246.98 | Si10 | 523.85 | 246.26 | Si10 | 483.72 | 199.85 | Si10 | 499.29 | 239.73 |
| C11 | 189.46 | 869.46 | C11 | 41.99 | 450.79 | C11 | 101.33 | 255.92 | Si11 | 489.34 | 193.56 |
| C12 | 163.30 | 248.93 | C12 | 150.26 | 201.04 | C12 | 176.60 | 132.36 | C12 | 90.29 | 277.60 |
| Si13 | 373.25 | 687.25 | Si13 | 304.33 | 643.70 | Si13 | 345.75 | 559.38 | C13 | 142.44 | 239.05 |
| Si14 | 544.67 | 510.68 | Si14 | 539.28 | 231.36 | Si14 | 535.26 | 143.36 | Si14 | 389.23 | 548.80 |
| C15 | 196.90 | 334.31 | C15 | 137.89 | 193.28 | C15 | 113.18 | 109.43 | Si15 | 544.59 | 166.48 |
| C16 | 192.79 | 184.43 | C16 | 136.32 | 208.91 | C16 | 117.08 | 146.66 | C16 | 182.09 | 31.89 |
| Cr17 | 1646.59 | 1918.12 | Cr17 | 1476.36 | 730.92 | Cr17 | 517.01 | 741.00 | C17 | 103.83 | 150.02 |
| Si18 | 575.54 | 291.55 | Si18 | 566.03 | 155.74 | Si18 | 514.70 | 205.33 | Cr18 | 764.59 | 702.10 |
| C19 | 1082.64 | 2011.82 | C19 | 363.01 | 780.24 | C19 | 4.24 | 207.97 | Si19 | 511.00 | 240.22 |
| C20 | 116.36 | 260.39 | C20 | 104.67 | 277.16 | C20 | 154.36 | 46.40 | C20 | 13.33 | 227.08 |
| Si21 | 36.22 | 1571.94 | Si21 | 176.40 | 1500.01 | Si21 | 251.80 | 251.80 | C21 | 107.55 | 192.71 |
| Si22 | 531.76 | 369.24 | Si22 | 535.93 | 394.12 | Si22 | 450.06 | 63.77 | Si22 | 308.33 | 1275.13 |
| C23 | 228.64 | 145.86 | C23 | 232.87 | 141.85 | C23 | 227.25 | 111.12 | Si23 | 461.15 | 65.07 |
| C24 | 183.46 | 172.73 | C24 | 151.86 | 199.96 | C24 | 191.44 | 116.70 | C24 | 227.05 | 125.36 |
| Si25 | 471.57 | 306.05 | Si25 | 540.10 | 238.99 | Si25 | 545.51 | 106.06 | C25 | 200.46 | 97.00 |
| Si26 | 303.83 | 735.31 | Si26 | 308.26 | 655.23 | Si26 | 322.17 | 615.50 | Si26 | 529.98 | 188.28 |
| C27 | 182.23 | 661.12 | C27 | 114.36 | 596.13 | C27 | 27.29 | 430.20 | Si27 | 327.81 | 585.94 |

| CO→CrSiC | | | $CO_2$→CrSiC | | | NO→CrSiC | | | $NO_2$→CrSiC | | |
|---|---|---|---|---|---|---|---|---|---|---|---|
| **Atom** | **σ iso** | **σ aniso** | **Atom** | **σ iso** | **σ aniso** | **Atom** | **σ iso** | **σ aniso** | **Atom** | **σ iso** | **σ aniso** |
| C28 | 28.64 | 197.05 | C28 | 16.46 | 204.02 | C28 | 109.07 | 585.55 | C28 | 37.54 | 440.43 |
| Si29 | 297.22 | 498.06 | Si29 | 361.05 | 214.16 | Si29 | 121.72 | 330.23 | C29 | 75.39 | 515.50 |
| Si30 | 563.49 | 580.44 | Si30 | 363.06 | 232.65 | Si30 | 155.69 | 394.74 | Si30 | 237.30 | 336.69 |
| C31 | 48.10 | 367.94 | C31 | 100.25 | 285.00 | C31 | 117.12 | 159.56 | Si31 | 168.97 | 275.50 |
| Si32 | 371.21 | 1553.42 | Si32 | 183.00 | 1517.43 | Si32 | 226.73 | 1109.67 | C32 | 171.25 | 22.52 |
| | | | O33 | 132.27 | 224.08 | | | | Si33 | 298.37 | 782.29 |

"Isotropic chemical-shielding" ( $\sigma_{iso}$) "anisotropic chemical-shielding" ( $\sigma_{aniso}$ ) [51]: $\sigma_{iso} = \frac{\sigma 33 + \sigma 22 + \sigma 11}{3}$;

$$\sigma_{aniso} = \sigma 33 - \frac{\sigma 22 + \sigma 11}{2}$$

The resulting graphs of "NMR" data in Table 2 have shown approximately identical chemical shielding behavior of isotropic and anisotropy factors of GM→CrSiC with several sharp peaks related to carbon, nitrogen, oxygen, silicon, and chromium of gas molecules (adsorbate) and TM-doped SiC nanosheet (adsorbent) in the active site situations. CO→CrSiC with several sharp peaks related to the adsorption site for atoms including C1, C7, C11, C19, C28, Si4, Si21, Si29, Si30, Cr17; $CO_2$→CrSiC with several sharp peaks for atoms of C7, C11, C19, C28, Si13, Si21, Si29, Si30, Cr17; NO→CrSiC with several sharp peaks for atoms of O1, N2, Cr17 and several less sharped peaks for atoms of C5, C8, C28, Si13, Si26; and $NO_2$→CrSiC with several sharp peaks for atoms of O3, Si14, Si22, Si27, Si30, Si31, and several less sharper peaks of N1, C6, Cr18, respectively, have been indicated (Table 2).

In NMR spectroscopy, remarkable peaks around silicon and chromium atoms in the SiC nanosheets are observed during the adsorption of gas molecules; however, there are fluctuations in the chemical shielding behavior, with both isotropic and anisotropic components.

*3.4. Vibrations of gas adsorption onto Cr-doped SiC monolayer.*

In this part, the stability of complexes, including gas adsorption on a chromium (Cr)-doped graphene-like silicon carbide (SiC) monolayer sheet, has been investigated using thermodynamic properties that define the reactions undergone by CO, $CO_2$, NO, and $NO_2$ within the CrSiC coordination sphere.

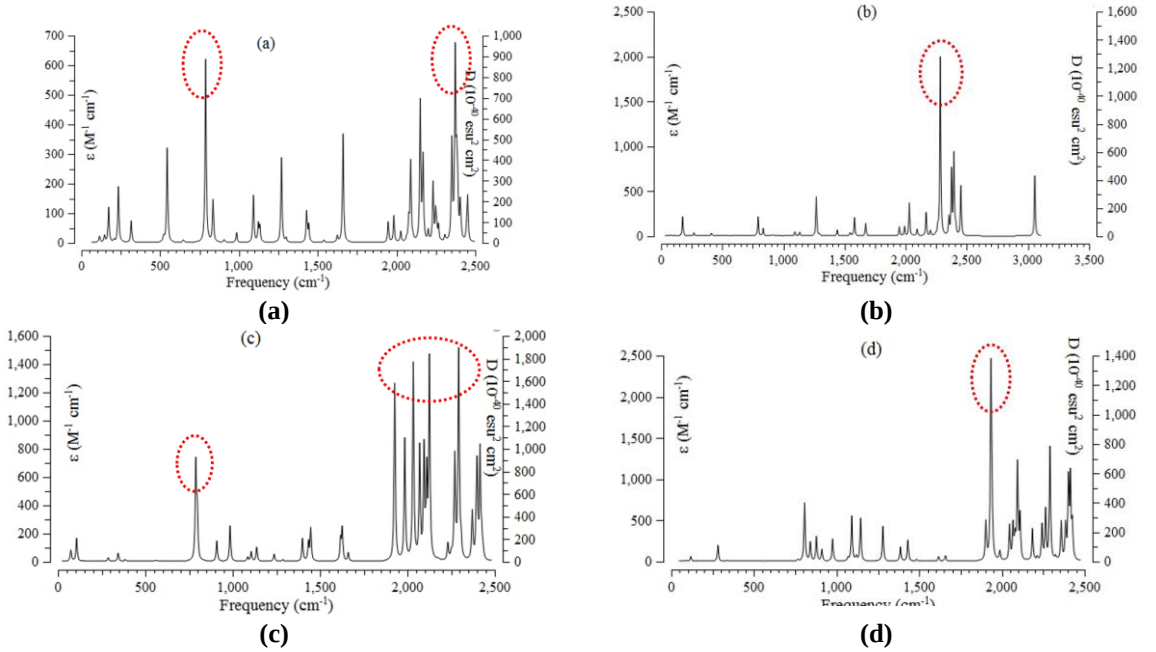


**Figure 4.** The frequency ($cm^{-1}$) changes through the "IR" spectrums for **(a)** CO→CrSiC; **(b)** $CO_2$→CrSiC; **(c)** NO→CrSiC; **(d)** $NO_2$→CrSiC as the selective gas detectors.

Regarding the adsorption process, the thermodynamic characteristics of CO, CO2, NO, and NO2 adsorption on the surface of CrSiC were evaluated as gas detectors, which can be used as selective adsorbents for these gases (Table 3).

Furthermore, the IR spectra for the adsorption of CO, $CO_2$, NO, and $NO_2$ on the surfaces of CrSiC have been reported in Figure 4 (a-d). The graph in Figure 4(a) shows a frequency range of 500 cm-1 to 2500 cm-1 for the complex CO→CrSiC, with several sharp peaks at 544.14 $cm^{-1}$, 788.20 $cm^{-1}$, 1269.6 $cm^{-1}$, 1660.33 $cm^{-1}$, 2150.96 $cm^{-1}$, and 2372.32 $cm^{-1}$.

Figure 4 (b) shows several of the strongest IR peaks of $CO_2$→CrSiC, approximately between 1000 $cm^{-1}$ and 3000 $cm^{-1}$, with a sharp peak of around 2029.61 $cm^{-1}$. Figure 4(c) shows several weaker IR peaks of NO→CrSiC, approximately between 550 $cm^{-1}$ and 2500 $cm^{-1}$, with several considerable peaks around 1927.38$cm^{-1}$, 1985.13 $cm^{-1}$, 2033.32 $cm^{-1}$, 2070.30 $cm^{-1}$, 2094.94, 2110.71 $cm^{-1}$, 2125.89 $cm^{-1}$, 2270.87 $cm^{-1}$, 20293.92 $cm^{-1}$, and 2416.07 $cm^{-1}$. Figure 4(d) exhibits several weaker IR peaks of $NO_2$→CrSiC, approximately between 550 $cm^{-1}$ and 2500 $cm^{-1}$, with several sharp peaks around 1091.68 $cm^{-1}$, 1144.68 $cm^{-1}$, 1933.85 $cm^{-1}$, 2094.63 $cm^{-1}$, 2290.29 $cm^{-1}$, 2402.25 $cm^{-1}$, and 2413.97$cm^{-1}$.

The adsorptive capacity of CO, $CO_2$, NO, and $NO_2$ on the surface of CrSiC is approved by the $\Delta E^o_{ads}$ amounts as follows:

$$\Delta E^o_{ads} = \Delta E^o_{X\rightarrow CrSiC} - (\Delta E^o_X + \Delta E^o_{CrSiC}); (X=CO, CO_2, NO, NO_2) \quad (5)$$

Table 3 shows that the adsorption of CO, $CO_2$, NO, and $NO_2$ on the surface of CrSiC must have both "physical" and "chemical" nature. All the measured relative adsorption energies ($\Delta E^o_{ads}$) are almost identical and exhibit the agreement of the estimated data by all methods and the accuracy of the calculations. In fact, CrSiC has a higher interaction energy from Van der Waals' forces with gas molecules, including CO, $CO_2$, NO, and $NO_2$, that can make it highly stable.

**Table 3.** The thermodynamic character of CO, $CO_2$, NO, and $NO_2$ adsorbed on the CrSiC as the selective gas adsorbents.

| Compound | $\Delta E^o \times 10^{-4}$ (kcal/mol) | $\Delta H^o \times 10^{-4}$ (kcal/mol) | $\Delta G^o \times 10^{-4}$ (kcal/mol) | $S^o$ (Cal/K.mol) | Dipole moment (Debye) |
|---|---|---|---|---|---|
| SiC | –304.3389 | –304.3389 | –304.3417 | 93.684 | 9.6011 |
| CrSiC | –351.2309 | –351.2308 | –351.2335 | 90.931 | 9.6048 |
| CO | –6.9784 | –6.9784 | –6.9798 | 47.100 | 0.2373 |
| $CO_2$ | –11.6121 | –11.6121 | –11.6136 | 51.378 | 0.0000 |
| NO | –8.0017 | –8.0016 | –8.0031 | 48.968 | 0.2376 |
| $NO_2$ | –12.6298 | –12.6298 | –12.6315 | 57.792 | 0.2323 |
| CO→CrSiC | –358.2348 | –358.2348 | –358.2377 | 98.812 | 11.1282 |
| $CO_2$→CrSiC | –362.8914 | –362.8913 | –362.8942 | 98.041 | 10.1381 |
| NO→CrSiC | –359.2746 | –359.2746 | –359.2776 | 101.641 | 8.5831 |
| $NO_2$→CrSiC | –363.8979 | –363.8978 | –363.9006 | 94.975 | 8.3460 |

Furthermore, the difference of $\Delta H_R$ among adsorption of CO, $CO_2$, NO, and $NO_2$ on the surface of Cr–doped SiC has been unraveled due to non-covalent binding resulting from interatomic interactions between gas molecules and surface (GM→CrSiC) and covalent binding resulting from intra-atomic interactions between the transition metal of chromium and silicon carbide nanosheet (CrSiC) (Table 3).

For the adsorption mechanism, $\Delta G^o_{ads}$ is calculated as follows:

$$\Delta G^o_{ads} = \Delta G^o_{X\rightarrow CrSiC} - (\Delta G^o_X + \Delta G^o_{CrSiC}); (X=CO, CO_2, NO, NO_2) \quad (6)$$

Based on the data in Table 3, it is predicted that gas adsorption on the CrSiC surface may have both physical and chemical origins. As shown in Table 3, all the computed $\Delta G^{o}_{ads}$ amounts are close, which exhibits the agreement of the evaluated data by all methods and the validity of the computations.

However, the CrSiC surface appears to be sufficiently efficient for the adsorption of gas molecules containing CO, $CO_2$, NO, and $NO_2$, driven by charge transfer from nitrogen and oxygen to the chromium-doped silicon carbide, facilitated by intra-atomic and interatomic interactions.

## 4. Conclusions

In summary, the nonmetal element-doped SiC nanosheet has been studied by first-principles calculations. Different dopants of gas molecules and doping sites are considered. The current research aims to remark on the illustration of gas adsorption on CrSiC nanosheet. Particularly, the structural, energetic, and infrared adsorption properties of linearly "atop" for CO, $CO_2$, NO, and $NO_2$ gas molecules adsorbing on CrSiC nanosheet have been explored by using DFT calculations. The changes in charge density indicate a more significant charge transfer in the CrSiC nanosheet, which acts as the electron acceptor, while gas molecules act as stronger electron donors through adsorption on the CrSiC nanosheet surface. It has been assumed that the priority for selecting the surface binding of the N-atom of NO, and O-atom of $NO_2$, CO, and $CO_2$ in the adsorption site can be impacted by the existence of close atoms in the CrSiC surface. In fact, the Cr site in SiC nanosheet has a higher interaction energy from Van der Waals' forces with gas molecules, including CO, $CO_2$, NO, and $NO_2$, that can make them highly stable. Finally, our molecular simulation results have exhibited the existence of orbital hybridization between the chromium site and gas molecules of CO, $CO_2$, NO, and $NO_2$, which also supports the recovery of adsorption susceptibility of the graphene sheet. In fact, the CrSiC surface can promise an applicable outlook in the field of CO, $CO_2$, NO, and $NO_2$ gas adsorbents. This research is a preliminary material study with potential for gas sensing after further validation.

### Institutional Review Board Statement

Not applicable.

### Informed Consent Statement

Not applicable.

### Data Availability Statement

Not applicable.

### Funding

This research received no external funding.

## Acknowledgments

The author is grateful to Kastamonu University for successfully completing this paper and its research.

## Conflict of Interest

The author declares no conflict of interest.

## References

1. Myers, N.M.; Peña, F.J.; Cortés, N.; Vargas, P. Multilayer Graphene as an Endoreversible Otto Engine. *Nanomaterials* **2023**, *13*, 1548, https://doi.org/10.3390/nano13091548.
2. Irzhak, A.; Irzhak, D.; Kononenko, O.; Pundikov, K.; Roshchupkin, D. Changes in the Raman Spectrum of Monolayer Graphene under Compression/Stretching Strain in Graphene/Piezoelectric Crystal Structures. *Nanomaterials* **2023**, *13*, 350, https://doi.org/10.3390/nano13020350.
3. Rabchinskii, M.K.; Sysoev, V.V.; Ryzhkov, S.A.; Eliseyev, I.A.; Stolyarova, D.Y.; Antonov, G.A.; Struchkov, N.S.; Brzhezinskaya, M.; Kirilenko, D.A.; Pavlov, S.I. A blueprint for the synthesis and characterization of thiolated graphene. *Nanomaterials* **2021**, *12*, 45, https://doi.org/10.3390/nano12010045.
4. Bizyaev, I.; Gabdullin, P.; Chumak, M.; Babyuk, V.; Davydov, S.; Osipov, V.; Kuznetsov, A.; Kvashenkina, O.; Arkhipov, A. Low-Field Electron Emission Capability of Thin Films on Flat Silicon Substrates: Experiments with Mo and General Model for Refractory Metals and Carbon. *Nanomaterials* **2021**, *11*, 3350, https://doi.org/10.3390/nano11123350.
5. Tene, T.; Guevara, M.; Bonilla García, N.; Borja, M.; Vacacela Gomez, C. Modeling 2D Arrangements of Graphene Nanoribbons. *Crystals* **2023**, *13*, 311, https://doi.org/10.3390/cryst13020311.
6. Politano, G.G.; Versace, C. Recent Advances in the Raman Investigation of Structural and Optical Properties of Graphene and Other Two-Dimensional Materials. *Crystals* **2023**, *13*, 1357, https://doi.org/10.3390/cryst13091357.
7. Li, L.; Zhou, M.; Jin, L.; Mo, Y.; Xu, E.; Chen, H.; Liu, L.; Wang, M.; Chen, X.; Zhu, H. Green Preparation of Aqueous Graphene Dispersion and Study on Its Dispersion Stability. *Materials* **2020**, *13*, 4069, https://doi.org/10.3390/ma13184069.
8. Lim, J.-Y.; Jang, H.-S.; Yoo, H.-J.; Kim, S.-i.; Whang, D. Pattern Pick and Place Method for Twisted Bi- and Multi-Layer Graphene. *Materials* **2019**, *12*, 3740, https://doi.org/10.3390/ma12223740.
9. Liang, F.; Zhan, L.; Guo, T.; Wu, X.; Chu, J. CVD-Grown 2D Nonlayered NiSe as a Broadband Photodetector. *Micromachines* **2021**, *12*, 1066, https://doi.org/10.3390/mi12091066.
10. Mollaamin, F.; Monajjemi, M. Doping of Graphene Nanostructure with Iron, Nickel and Zinc as Selective Detector for the Toxic Gas Removal: A Density Functional Theory Study. *C–Journal of Carbon Research* **2023**, *9*, 20, https://doi.org/10.3390/c9010020.
11. Mollaamin, F. Anchoring of 2D layered materials of $Ge_5Si_5O_{20}$ for (Li/Na/K)-(Rb/Cs) batteries towards Eco-friendly energy storage. *BMC Chemistry* **2025**, *19*, 233, https://doi.org/10.1186/s13065-025-01593-0.
12. Mollaamin, F.; Monajjemi, M. Graphene Embedded with Transition Metals for Capturing Carbon Dioxide: Gas Detection Study Using QM Methods. *Clean Technol.* **2023**, *5*, 403–417, https://doi.org/10.3390/cleantechnol5010020.
13. Mollaamin, F.; Monajjemi, M. Transition metal (X = Mn, Fe, Co, Ni, Cu, Zn)-doped graphene as gas sensor for $CO_2$ and $NO_2$ detection: a molecular modeling framework by DFT perspective. *J. Mol. Model* **2023**, *29*, 119, https://doi.org/10.1007/s00894-023-05526-3.
14. Mollaamin, F.; Monajjemi, M. Tailoring and functionalizing the graphitic-like GaN and GaP nanostructures as selective sensors for NO, $NO_2$, and $NH_3$ adsorbing: a DFT study. *J. Mol. Model* **2023**, *29*, 170, https://doi.org/10.1007/s00894-023-05567-8.
15. Jiang, L.; Dong, Y.; Cui, Z. Adsorption of Metal Atoms on SiC Monolayer. *Inorganics* **2023**, *11*, 240. https://doi.org/10.3390/inorganics11060240.
16. Min, S.-J.; Shin, M.C.; Thi Nguyen, N.; Oh, J.-M.; Koo, S.-M. High-Performance Temperature Sensors Based on Dual 4H-SiC JBS and SBD Devices. *Materials* **2020**, *13*, 445, https://doi.org/10.3390/ma13020445.

17. Yang, X.; Liu, R.; Liu, B.; Liu, M. Synthesis of Ultra-Thin Two-Dimensional SiC Using the CVD Method. *Energies* **2022**, *15*, 6351, https://doi.org/10.3390/en15176351.
18. Zhou, H.; Chen, Z.; Kountoupi, E.; Tsoukalou, A.; Abdala, P.M.; Florian, P.; Fedorov, A.; Müller, C.R. Two-dimensional molybdenum carbide 2D-Mo2C as a superior catalyst for $CO_2$ hydrogenation. *Nat. Commun.* **2021**, *12*, 5510, https://doi.org/10.1038/s41467-021-25784-0.
19. Mollaamin, F.; Monajjemi, M. An Architectural Battery Designed by Substituting Lithium with Second Main Group Metals (Be, Mg, Ca/Cathode) and Hybrid Oxide of Fourth Group Ones (Si, Ge, Sn/Anode) Nanomaterials Towards $H_2$ Adsorption: A Computational Study. *Nanomaterials* **2025**, *15*, 959, https://doi.org/10.3390/nano15130959.
20. Belarouci, S.; Ouahrani, T.; Benabdallah, N.; Morales-García, Á.; Belabbas, I. Two-dimensional silicon carbide structure under uniaxial strains, electronic and bonding analysis. *Comput. Mater. Sci.* **2018**, *151*, 288–295, https://doi.org/10.1016/j.commatsci.2018.05.020.
21. Majid, A.; Akhtar, S.-e.-A.; Sandhu, Q.-u.-A.; Khan, M.I. Iodide Adsorption on Transition-Metal-Doped SiC Monolayers: A Density Functional Theory Based Bonding Analysis. *J. Electron. Mater.* **2021**, *50*, 3546-3556, https://doi.org/10.1007/s11664-021-08876-x.
22. Li, C.; Li, D.; Zhang, L.; Zhang, Y.; Zhang, L.; Gong, C.; Zhang, J. Boosted microwave absorption performance of transition metal doped TiN fibers at elevated temperature. *Nano Res.* **2023**, *16*, 3570-3579, https://doi.org/10.1007/s12274-023-5398-3.
23. Singh, R.S. $CO_2$ Capture by Metal-Decorated Silicon Carbide Nanotubes. *Silicon* **2023**, *15*, 4501–4511, https://doi.org/10.1007/s12633-023-02368-9.
24. Ahmed, H.; Hashim, A. Structural, Optical and Electronic Properties of Silicon Carbide Doped PVA/NiO for Low Cost Electronics Applications. *Silicon* **2021**, *13*, 1509–1518, https://doi.org/10.1007/s12633-020-00543-w.
25. Soliman, K.A.; Aal, S.A. The efficiency of n- and p-type doping silicon carbide nanocage toward ($NO_2$, $SO_2$, and $NH_3$) gases. *Chem. Pap.* **2022**, *76*, 4835–4853, https://doi.org/10.1007/s11696-022-02183-3.
26. Qin, T.; Wang, Z.; Wang, Y.; Besenbacher, F.; Otyepka, M.; Dong, M. Recent progress in emerging two-dimensional transition metal carbides. *Nano-Micro Lett.* **2021**, *13*, 183, https://doi.org/10.1007/s40820-021-00710-7.
27. Dippong, T. Cadar, O. Levei, E.A. Effect of Transition Metal Doping on the Structural, Morphological, and Magnetic Properties of $NiFe_2O_4$. *Materials* **2022**, *15*, 2996, https://doi.org/10.3390/ma15092996.
28. Roccaforte, F.; Fiorenza, P.; Vivona, M.; Greco, G.; Giannazzo, F. Selective Doping in Silicon Carbide Power Devices. *Materials* **2021**, *14*, 3923, https://doi.org/10.3390/ma14143923.
29. Mollaamin, F. Investigating the Treatment of Transition Metals for Ameliorating the Ability of Boron Nitride for Gas Sensing & Removing: A Molecular Characterization by DFT Framework. *Prot. Met. Phys. Chem. Surf.* **2024**, *60*, 1050–1063, https://doi.org/10.1134/S2070205124702502.
30. Perdew, J.P.; Burke, K.; Ernzerhof, M. Generalized gradient approximation made simple. *Phys. Rev. Lett.* **1996**, *77*, 3865–3868, https://doi.org/10.1103/PhysRevLett.77.3865.
31. Mollaamin, F. Alkali Metals Doped on Tin-Silicon and Germanium-Silicon Oxides for Energy Storage in Hybrid Biofuel Cells: A First-Principles Study. *Russ. J. Phys. Chem. B.* **2024**, *19*, 720–734, https://doi.org/10.1134/S1990793125700393.
32. Mollaamin, F.; Monajjemi, M. Nanomaterials for Sustainable Energy in Hydrogen-Fuel Cell: Functionalization and Characterization of Carbon Nano-Semiconductors with Silicon, Germanium, Tin or Lead through Density Functional Theory Study. *Russ. J. Phys. Chem. B.* **2024**, *18*, 607–623, https://doi.org/10.1134/S1990793124020271.
33. Mollaamin, F.; Monajjemi, M. In Situ Ti-Embedded SiC as Chemiresistive Nanosensor for Safety Monitoring of CO, $CO_2$, NO, $NO_2$: Molecular Modelling by Conceptual Density Functional Theory. *Russ. J. Phys. Chem. B.* **2024**, *18*, 49–66,https://doi.org/10.1134/S1990793124010159.
34. Mollaamin, F. Competitive Intracellular Hydrogen-Nanocarrier Among Aluminum, Carbon, or Silicon Implantation: a Novel Technology of Eco-Friendly Energy Storage using Research Density Functional Theory. *Russ. J. Phys. Chem. B.* **2024**, *18*, 805–820, https://doi.org/10.1134/S1990793124700131.
35. Villeneuve-Faure, C.; Boumaarouf, A.; Shah, V.; Gammon, P.M.; Lüders, U.; Coq Germanicus, R. SiC Doping Impact during Conducting AFM under Ambient Atmosphere. *Materials* **2023**, *16*, 5401, https://doi.org/10.3390/ma16155401.

36. Mollaamin, F.; Shahriari, S.; Monajjemi, M.; Khalaj, Z. Nanocluster of Aluminum Lattice via Organic Inhibitors Coating: A Study of Freundlich Adsorption. *J. Clust. Sci.* **2023**, *34*, 1547–1562, https://doi.org/10.1007/s10876-022-02335-1.
37. Mollaamin, F.; Monajjemi, M. Graphene-based resistant sensor decorated with Mn, Co, Cu for nitric oxide detection: Langmuir adsorption & DFT method. *Sensor Rev.* **2023**, *43*, 266–279, https://doi.org/10.1108/SR-03-2023-0040.
38. Mollaamin, F.; Monajjemi, M. Molecular modelling framework of metal-organic clusters for conserving surfaces: Langmuir sorption through the TD-DFT/ONIOM approach. *Mol. Simul.* **2023**, *49*, 365–376, https://doi.org/10.1080/08927022.2022.2159996.
39. Dennington, R.; Keith Todd, A.; Millam John, M. GaussView, Version 6.06.16. Semichem Inc., Shawnee Mission, KS, USA, **2016**.
40. Frisch, M.J.; Trucks, G.W.; Schlegel, H.B.; Scuseria, G.E.; Robb, M.A.; Cheeseman, J.R.; Scalmani, G.; Barone, V.; Petersson, G.A.; Nakatsuji, H.; Li, X.; Caricato, M.; Marenich, A.V.; Bloino, J.; Janesko, B.G.; Gomperts, R.; Mennucci, B.; Hratchian, H.P.; Ortiz, J. V.; Izmaylov, A. F.; Sonnenberg, J.L.; Williams-Young, D.; Ding, F.; Lipparini, F.; Egidi, F.; Goings, J.; Peng, B.; Petrone, A.; Henderson, T.; Ranasinghe, D.; Zakrzewski, V.G.; Gao, J.; Rega, N.; Zheng, G.; Liang, W.; Hada, M.; Ehara, M.; Toyota, K.; Fukuda, R.; Hasegawa, J.; Ishida, M.; Nakajima, T.; Honda, Y.; Kitao, O.; Nakai, H.; Vreven, T.; Throssell, K.; Montgomery, J.A., Jr.; Peralta, J.E.; Ogliaro, F.; Bearpark, M.J.; Heyd, J.J.; Brothers, E.N.; Kudin, K.N.; Staroverov, V.N.; Keith, T.A.; Kobayashi, R.; Normand, J.; Raghavachari, K.; Rendell, A.P.; Burant, J.C.; Iyengar, S.S.; Tomasi, J.; Cossi, M.; Millam, J.M.; Klene, M.; Adamo, C.; Cammi, R.; Ochterski, J.W.; Martin, R.L.; Morokuma, K.; Farkas, O.; Foresman, J.B.; Fox, D.J. Gaussian 16, Revision C.01, Gaussian, Inc., Wallingford CT, **2016**.
41. Romano, F.; Milluzzo, G.; Di Martino, F.; D'Oca, M.C.; Felici, G.; Galante, F.; Gasparini, A.; Mariani, G.; Marrale, M.; Medina, E. First characterization of novel silicon carbide detectors with ultra-high dose rate electron beams for FLASH radiotherapy. *Appl. Sci.* **2023**, *13*, 2986, https://doi.org/10.3390/app13052986.
42. Chatterjee, A.; Sen, S.; Paul, S.; Roy, P.; Seikh, A.H.; Alnaser, I.A.; Das, K.; Sutradhar, G.; Ghosh, M. Fabrication and Characterization of SiC-reinforced Aluminium Matrix Composite for Brake Pad Applications. *Metals* **2023**, *13*, 584, https://doi.org/10.3390/met13030584.
43. Zhang, M.; Huang, J.; Liu, X.; Lin, L.; Tao, H. Electronic Structure and High Magnetic Properties of (Cr, Co)-codoped 4H–SiC Studied by First-Principle Calculations. *Crystals* **2020**, *10*, 634, https://doi.org/10.3390/cryst10080634.
44. Su, Z.-C.; Li, Y.-H.; Lin, C.-F. Mid-Infrared Response from Cr/n-Si Schottky Junction with an Ultra-Thin Cr Metal. *Nanomaterials* **2022**, *12*, 1750, https://doi.org/10.3390/nano12101750.
45. Ishibashi, R.; Hayashi, Y.; Bo, H.; Kondo, T.; Hinoki, T. Radiation Effect in Ti-Cr Multilayer-Coated Silicon Carbide under Silicon Ion Irradiation up to 3 dpa. *Coatings* **2022**, *12*, 832, https://doi.org/10.3390/coatings12060832.
46. Jin, C.G.; Wu, X.M.; Zhuge, L.J.; Sha, Z.D.; Hong, B. Electric and magnetic properties of Cr-doped SiC films grown by dual ion beam sputtering deposition. *J. Phys. D: Appl. Phys.* **2008**, *41*, 035005, https://doi.org/10.1088/0022-3727/41/3/035005.
47. Trontelj, Z.; Pirnat, J.; Jazbinšek, V.; Lužnik, J.; Srčič, S.; Lavrič, Z.; Beguš, S.; Apih, T.; Žagar, V.; Seliger, J. Nuclear Quadrupole Resonance (NQR)—A Useful Spectroscopic Tool in Pharmacy for the Study of Polymorphism. *Crystals* **2020**, *10*, 450, https://doi.org/10.3390/cryst10060450.
48. Gregorovič, A. Quantitative Analysis of Hydration Using Nitrogen−14 Nuclear Quadrupole Resonance. *Anal. Chem.* **2015**, *87*, 6912–6918, https://doi.org/10.1021/acs.analchem.5b01492.
49. Kyriakidou, G.; Jakobsson, A.; Althoefer, K.; Barras, J. Batch-Specific Discrimination Using Nuclear Quadrupole Resonance Spectroscopy. *Anal. Chem.* **2015**, *87*, 3806–3811, https://doi.org/10.1021/ac5044658.
50. Budker, D.; Romalis, M. Optical magnetometry. *Nat. Phys.* **2007**, *3*, 227–234, https://doi.org/10.1038/nphys566.
51. Faulkner, R.A.; DiVerdi, J.A.; Yang, Y.; Kobayashi, T.; Maciel, G.E. The Surface of Nanoparticle Silicon as Studied by Solid-State NMR. *Materials* **2013**, *6*, 18–46, https://doi.org/10.3390/ma6010018.

## Publisher's Note & Disclaimer